



Quenching attenuation and fluorescence augmentation using plasmonic gold nanourchin and dielectric photonic crystal hybrid interface for mercury sensing

WEINAN LIU,^{1,2,†}  SEEMESH BHASKAR,^{1,2,4,†}  WEIJING WANG,^{2,3}
JOSEPH TIBBS,^{2,3} AND BRIAN T. CUNNINGHAM^{1,2,3,4,5,6,*}

¹Department of Electrical and Computer Engineering, University of Illinois at Urbana-Champaign, Urbana, IL 61801, USA

²Nick Holonyak Jr. Micro and Nanotechnology Laboratory, University of Illinois at Urbana-Champaign, Urbana, IL 61801, USA

³Department of Bioengineering, University of Illinois at Urbana-Champaign, Urbana, IL 61801, USA

⁴Carl R. Woese Institute for Genomic Biology, University of Illinois at Urbana-Champaign, Urbana, IL 61801, USA

⁵Department of Chemistry, University of Illinois at Urbana-Champaign, Urbana, IL 61801, USA

⁶Cancer Center at Illinois, Urbana, IL 61801, USA

†These authors contributed equally.

*bcunning@illinois.edu

Abstract: Photonic crystal enhanced fluorescence has emerged as a versatile technology for environmental and human health monitoring owing to high sensitivity provided by fluorescence emission amplification, lifetime reduction, and collection efficiency improvement. When plasmonic nanoparticles are used in combination with photonic crystal surfaces to provide fluorescence-enhancing photonic-plasmonic resonator hybrids, quenching phenomena observed in the ‘zone of inactivity’ represent a performance bottleneck. In particular, although plasmonic Au is an excellent plasmonic material for fluorescence enhancement, its use requires the incorporation of a spacer layer to circumvent quenching effects. In this work, we exploit the properties of the radiating guided mode resonance (GMR) model and sharp-edged plasmonic Au nano-urchins (AuNUs) to realize suppressed quenching and augmented fluorescence output without the use of an optical prism or microscope objective. Rigorous coupled-wave analysis (RCWA) and finite element method (FEM) analysis are used to provide insights corroborating experimentally observed 100-fold dequenched signal intensity. Multiphysics simulations of a fluorescent radiating dipole with different orientations and placements within the AuNU-PC system validate the experimentally observed polarization selectivity. The enhanced local density of states rendered by the synergistic coupling of core-tip plasmons of AuNUs and the GMR of the underlying photonic crystal were applied to demonstrate a 2 part-per-billion limit of detection for mercury (Hg^{2+}) ions, thereby presenting a representative example for a quench-free chem-biosensing interface under controlled conditions.

© 2026 Optica Publishing Group under the terms of the [Optica Open Access Publishing Agreement](#)

1. Introduction

Although fluorescence-based detection methodologies have emerged as gold standards in several disease diagnostic modalities [1,2], conventional fluorescence spectroscopy suffers from low signal collection efficiency, photobleaching, high background noise, low polarization selectivity and poor spectral resolution while requiring bulky optical components in the detection instrument [3–6]. The goal of developing practical fluorescence-based chemical and biological sensing for point-of-use (PoU) and point-of-care (PoC) applications demands miniaturization of associated

opto-electronic frameworks [7–9]. Photonic crystal enhanced fluorescence (PCEF) technology has emerged as a versatile tool to meet such demands on account of its ability to render lightweight and compact optical platforms with customizable interfacial functionalities [10–13]. A recent work presents an innovative solution to further simplify detection instruments that measure surface-based fluorescence emission by eliminating the bulky and expensive optical prisms and microscope objectives, in an approach called photonic crystal-coupled steering emission (PCSE) in which the excitation and collection mechanisms at the nano-micro-interface are precisely controlled [3]. Despite advances in manipulating fluorescence using PC interfaces [14,15], the lack of an efficient way to overcome the quenching encountered with the use of plasmonic gold (Au) nanoparticles as localized electromagnetic hotspot amplifiers serves as a roadblock to achieving superior fluorescent emission output [16–20]. Nevertheless, the high chemical stability, ease of bio-chemical functionalization, tunable optical resonance in the Vis-NIR part of the electromagnetic (EM) spectra, and high electron density ($\approx 5.90 \times 10^{16} \text{ m}^{-3}$) of plasmonic gold nanoparticles for fluorescence enhancement have led to their broad adoption [21–23]. Hence, there is a quandary of prerequisite to utilize the promising functionalities of plasmonic Au and simultaneously suppress the quenching in the so-called ‘zone of inactivity’ [18,24], in which fluorescent emitters within $\sim 5 \text{ nm}$ of the nanoparticle are dramatically quenched.

Several methods including, but not limited to (i) use of metal-dielectric decorated hybrids [16], (ii) hollow plasmonic AuNPs with void plasmons [25], (iii) Au nano-assemblies with Bragg plasmons [26], (iv) heterometallic hybrids of Au [27], and (v) porous Au nanomaterials [28] to name a few have been attempted to realize dequenched emission from AuNPs. The parasitic Ohmic losses and nonradiative decay of the emitter near the plasmonic surface results in surface induced quenching effects, which can be mitigated by separating the fluorophore and the AuNP with a spacer layer. Minute experimental artifacts in the fabrication of spacer configurations are known to induce unfavourable effects and quantitation inaccuracy in biosensing applications [26,29]. Moreover, the past investigations have been confined to the exploration of myriad nano-geometries over plasmonic thin films (as in SPR) which are inherently lossy [30,31]. In this background, utilizing PC-plasmonic hybrid interfaces to suppress the quenching in the near-field to realize dequenched and augmented far-field radiation is seldom explored.

In this work, we first present the applicability of hybrid coupling between plasmonic Au nanourchins (AuNUs) and a PC interface using rigorous coupled-wave analysis (RCWA) and finite element method (FEM) analysis. We then design, synthesize and experimentally demonstrate suppression in quenching while preserving the steering fluorescence output in the far-field using plasmonic AuNUs. While AuNUs are known to showcase bonding and antibonding plasmonic coupling, the core structure serves as an antenna (sustaining core plasmons), increasing the excitation cross sections and the electric field enhancements of the bonding plasmon modes thereby enhancing the effective dipole moment of tip plasmons [32–36]. The sharp tips and the interaction between them along with large surface area-to-volume ratios renders arguably the largest numbers of hotspots in AuNUs (as compared to nanospheres, nanorods, nanocubes nanotriangles etc.) [37,38] with intense electric field amplification upon irradiation to activate localized surface plasmon resonance (LSPR) [39]. Concomitantly, high local density of states (LDoS) is experienced by the plasmophores (fluorophores near the plasmonic surface) resulting in induced-plasmon effect of metal-enhanced fluorescence (MEF) [4,40,41].

Our approach synergistically harnesses the principle of the radiating plasmon model developed by Lakowicz et al. [42–44], as well as the radiating guided mode resonance (GMR) model [3,45] (recently developed by our team) where the emission from radiating dipoles is coupled to the far-field via the sub-wavelength localization properties of plasmonic excitations in the AuNUs as well as the GMR-coupling at the PC interface. We experimentally demonstrate a 100-fold fluorescence enhancement using bare AuNUs (without any spacer surface coating) with the PCSE platform in spite of surface-induced quenching. The boosted radiative decay rate of the proximal

radiating dipoles on account of the generation of hybridized resonances [46,47] and integrated hotspots [48,49] from metal (AuNU) - dielectric (PC substrate) framework is experimentally substantiated by rhodamine B and Hg^{2+} ions interaction measurements. While the experimental PCSE results are in accordance with the simulated results, the experimental measurements presenting the electronic transition probabilities corroborate the measured quenched and augmented fluorescence.

2. Methods

Figure 1(a) shows a conceptual layout of the optical setup used to capture the experimentally measured fluorescence. A typical surface plasmon-coupled emission (SPCE) and photonic crystal-coupled emission (PCCE) reporter molecule, rhodamine B, was utilized in all the experiments allowing straightforward comparisons with earlier reports [3,9,50]. Briefly, acetone, IPA, and Milli-Q water were used to rinse all of the PC substrates following cleaning with piranha solution. A spin coating technique was used to equally disperse the radiating dipoles (rhodamine B) throughout the surface of PC substrate. Two percent polyvinyl alcohol (PVA) polymer spin-coated at 3×10^3 rpm for 60 seconds produced ~ 65 nm thick overcoats; more information on fabrication is included in our recent works [3,45,50]. The PC substrates coated with radiating dipoles were excited using a 532 nm continuous wave (c.w.) laser, and the outcoupled emission was collected by a fiber optic (coupled to collimating lens) spectrometer (Ocean Optics 2000+) connected to Ocean Optics SpectraSuite software. A 550 nm long wave pass (LWP) filter was used to reduce the laser wavelength's intensity from entering the spectrometer and sheet polarizers (P1 and P2) were used to determine the input and output polarization selectivity of the PC substrates. Our recent work [3] scrutinized different PC engineering methods (thickness and refractive indices) for the system comprised of a 532 nm laser and rhodamine B fluorescent reporters. The substrate that presented an excellent overlap of the GMR of PC and the emission of the dye with the structural parameters ($\Lambda = 290$ nm, $t_1 = t_2 = t_3 = t_4 = 28$ nm, $d_1 = 110$ nm, $d_2 = 80$ nm, $d_3 = 60$ nm, $S_1 = 110$ nm, $S_2 = S_3 = S_4 = 190$ nm;) and the refractive indices of the glass (1.46), silicon nitride (2.03), titanium oxide (2.42), and the PVA (1.49) shown in Fig. 1(b) were chosen for all the experiments at the wavelength of interest. The transverse electric (TE) RCWA simulated dispersion diagram for this structure presents the counter-propagating guided modes of the PC with the zero-degree wavelength matching that of the emission maximum of the rhodamine B (~ 580 nm) [3]. COMSOL [51] simulations presenting the electric field hotspot intensity distribution of the AuNPs (size: 50 nm) and AuNUs (size: 65 nm, including spikes) are shown in Figs. 1(d)–1(g). The high field localization achieved in the sharp nano-protrusions and nano-curvatures of the nano-urchins as compared to that of nanospheres are clearly seen in Fig. 1(f), g. Moreover, the high spatial distribution of hotspots due to hybrid coupling of tip-plasmons with the GMR of the PC is observed in Fig. 1 g. We note that although similar systems of plasmonic AuNUs are being hybridized with other sharp interfaces, metallic thin films (as in SPR) and photonic crystals (Bragg mirrors, 2D and 3D PCs), the hotspots have been utilized for electrochemical, SERS, TERS and related spectroscopic methods [52–54]. However, interfacing them over grating-based PCs to yield quenching attenuation (due to AuNUs) and fluorescence augmentation (due to PCs) has not been reported previously to our knowledge.

The Turkevich technique [21,55] was used for the synthesis of AuNPs and the protocol used for the synthesis of AuNUs is detailed in the Supplement 1. The high uniformity of the PC grating interface is seen in the SEM image in Fig. 2(a). The AFM topographical image (2D in Fig. 2(b) and 3(D) in Fig. 2(d)) along with the line profile (Fig. 2(c)) indicates an ~ 30 nm depth of the grooves in accordance with earlier works [3]. The high-angle annular dark-field (HAADF) - transmission electron microscopy (TEM) images of the synthesized AuNUs is shown in Fig. 2(e) along with the elemental mapping image showing the presence of gold, oxygen and copper (with the copper signals originating from the underlying copper grid). The high-resolution

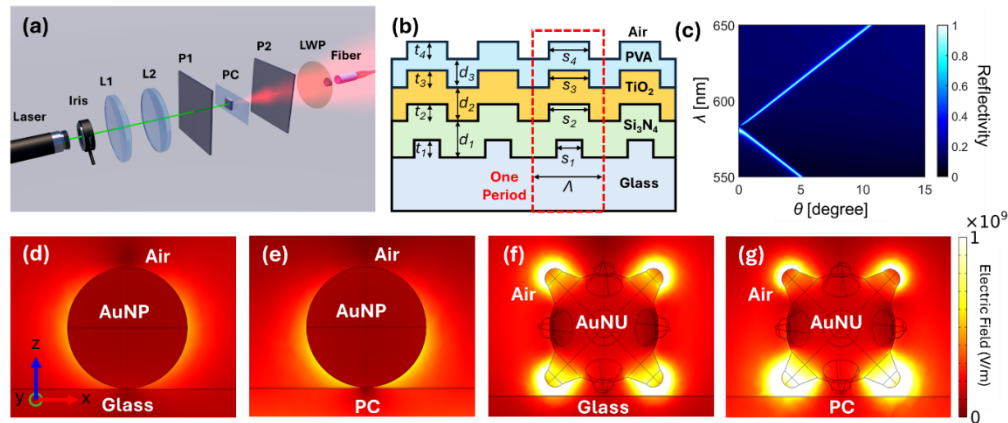


Fig. 1. Optical framework, dispersion diagram and plasmonic hotspot distribution. (a) Optical setup of the photonic crystal-coupled enhanced steering (PCES) emission platform. L1 and L2: collimating lenses, P1 and P2: polarizers, LWP: long wave pass filter, PC: photonic crystal. (b) The structural parameters of the PC. (c) RCWA simulated dispersion diagram of the PC. Electric field intensity obtained using COMSOL presenting the hotspots by interfacing the glass with (d) AuNP and (f) AuNU. Electric field intensity presenting the hotspots by interfacing the PC with the (e) AuNP and (g) AuNU.

(HR)-HRTEM image indicates d-spacing (which are characteristic lattice/atomic fringes) of metallic Au (yellow) in accordance with the reference code from the Inorganic Crystal Structure Database (ICSD) [Au: 98-061-1625]. The spectral mapping in Fig. 2(f), multiple TEM (Fig. 2 h) and HRTEM (Figs. 2(i) and 2(j)) images of the AuNUs confirm the elemental, morphological, and structural features.

The hybridization of AuNUs with the PC interface presents an ideal platform to simultaneously leverage the effectiveness of microscopic and mesoscopic strategies [29,56]. The former strategy is accomplished on account of light-matter interactions: (i) excellent overlap between the laser excitation and high excitation co-efficient of the radiating dipole, (ii) tunability of GMR of the PC to simultaneously match the emission of the radiating dipole and the LSPR of AuNUs, thereby supporting enhanced excitation and emission. The mesoscopic strategy is realized because of the: (i) *Physical effects*: This is attributed to the low-loss of the underlying all-dielectric PC substrate [57,58], and (ii) *Geometric effects*: This is attributed to the sharp-edged AuNUs' nano-protrusions, nano-voids and nano-crevices [56,59]. Such nanostructure protrusions have been the subject of wide exploration as they generate regions of high field confinement and local field enhancement, on account of their ability to create additional radiative decay channels [4,60]. Such synchronized effects from microscopic and mesoscopic strategies enables minimization of undesirable macroscopic elements to gather/collect more light using objectives and expensive lenses.

We performed simulation analysis to understand the effect of different polarizations of light as well as different orientations of radiating dipole on the glass and PC surface, with and without AuNPs (referring to spherical NPs) and AuNUs. Our simulations used finite element method (FEM) electromagnetic field solver COMSOL Multiphysics and demonstrated radiating dipoles, positioned upon a PC or glass substrate. The 3D simulation was performed within a cuboid space of $11\Lambda \times \Lambda \times 10\Lambda$. A dipole point source with an emission wavelength of 580 nm was placed at the ridge center of the PC or the glass substrate, and all domains of the model were selected as far-field domains to enable far-field calculation of the radiation patterns. The simulations were conducted with a single dipole aligned along three orthogonal orientations:

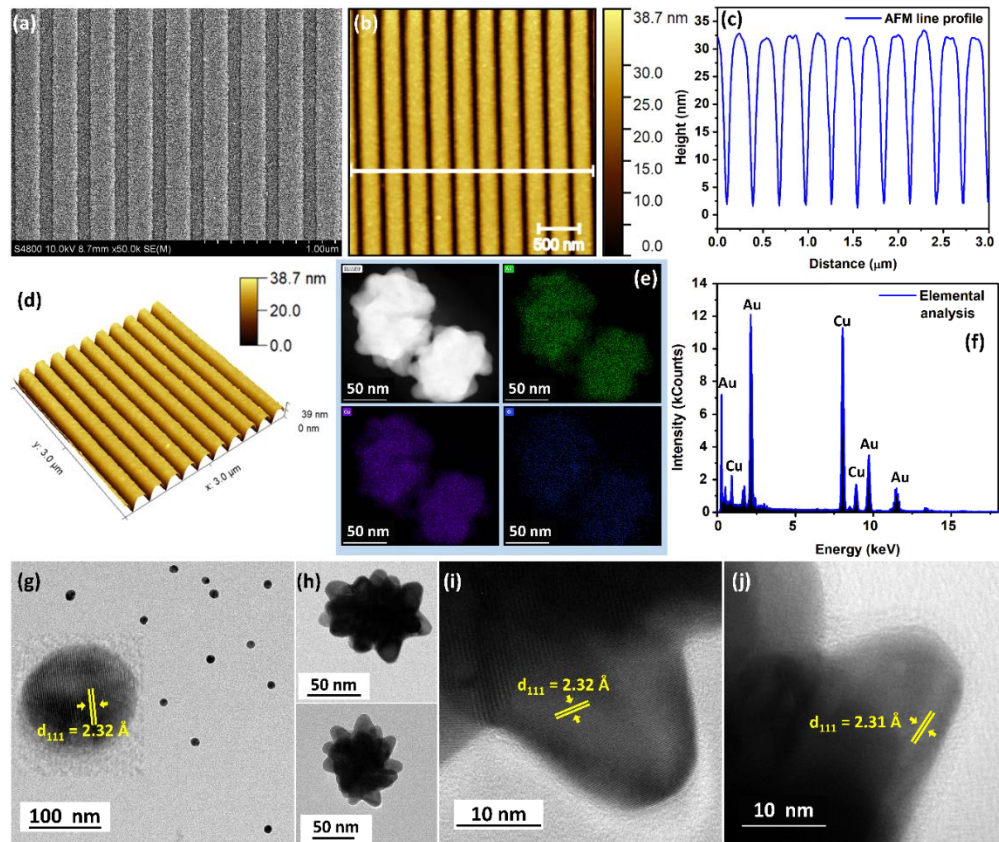


Fig. 2. PC substrate and plasmonic nanomaterial characterization. (a) SEM, (b) AFM image and (c) AFM height profile, (d) 3D AFM image of the PC substrate. (e) TEM Elemental mapping analysis of the AuNUs along with the spectra shown in (f). (g) TEM image of AuNP shown with HRTEM image. (h) Multiple TEM images of AuNUs. (i) HRTEM image of AuNUs showcasing the lattice fringes characteristic to that of gold.

along the x -axis, i.e. along the periodic direction of the PC; along the z -axis, perpendicular to the PC surface; and along the y -axis, parallel to the PC surface but perpendicular to the x - z plane. All three orientations of the dipoles need to be considered on account of the intricate dependence on polarization selectivity in the near-field region of the dipole and so as to mimic the experimentally observed results, where the emitter (rhodamine B) is isotropically emitting in the homogeneously distributed polymer matrix. The quenching and dequenching effect of AuNP and AuNU were studied via setting a AuNP or AuNU 1 nm above the PC and the dipole, followed by calculation of their corresponding radiated near- and far-field. The y -oriented dipole directly provides the electric field component polarized perpendicular to the plane of incidence and is referred to as $|E_{TE}|^2$ (Figs. 3(a)–3(c)). The sum of the field intensity calculated from the x - (Figs. 3(d)–3(f)) and z -oriented (Figs. 3(g)–3(i)) dipoles contributes to the electric field component of the emitted radiation polarized parallel with the plane of incidence and is referred to as $|E_{TM}|^2$. TE- and TM-polarized PC-coupled emissions in our experiments correspond to the electric field components $|E_{TE}|^2$ and $|E_{TM}|^2$ computed in the far-field, respectively [61–63]. The coupling between the dipole emission to the PC guided mode was validated through the log-scale electric field and Poynting vector calculation within the x - z plane, as shown in the Supplement 1 Figure S1. The radiating dipole with 580 nm emission was chosen to mimic the experimental

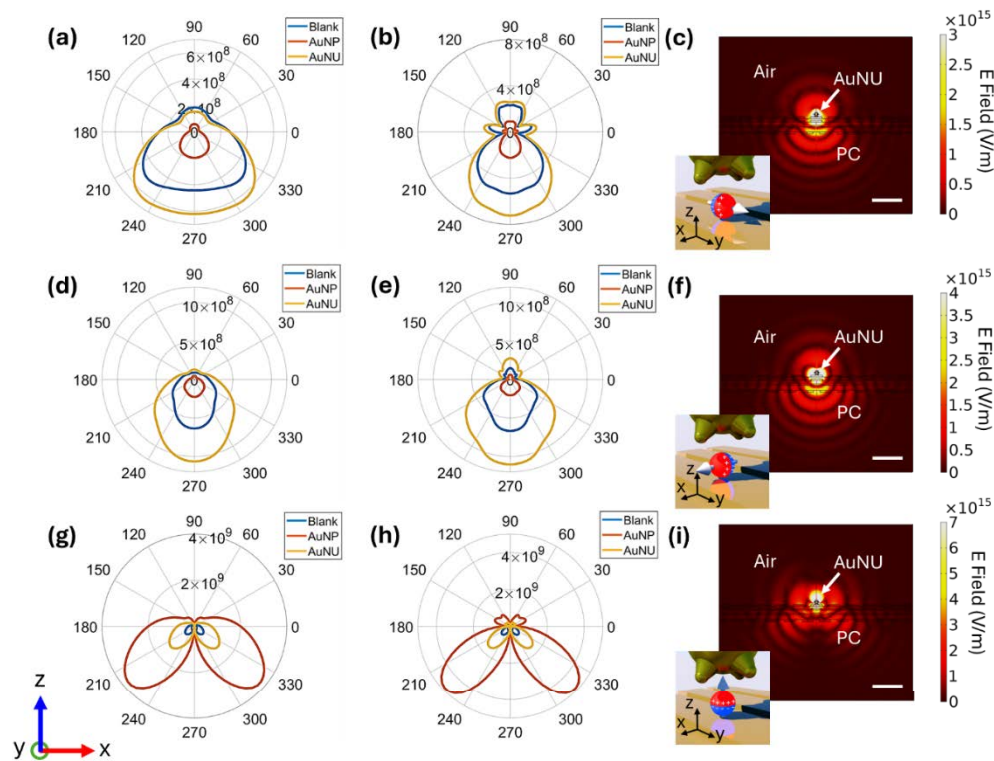


Fig. 3. Simulated radiating dipole coupling with the glass and PC interfaces. Far-field pattern of the y -oriented dipole placed on (a) glass and (b) PC with blank, AuNP, AuNU configurations, respectively. (c) Near-field electric field distribution in the x - z plane of a dipole set in between PC and a AuNU 1 nm above. (d)–(f) and (g)–(i) are corresponding figures for x -oriented and z -oriented dipoles, respectively. The insets of figures (c), (f), and (i) illustrate the position (on PC) and orientation of the dipoles where a AuNU is on the top.

scenario (as rhodamine has emission maximum at ~ 580 nm) [64]. In our simulation, an electric current dipole moment of $1 \text{ A} \cdot \text{m}$ magnitude was applied as the radiation source, and the result was calculated within the near field ($< 1 \mu\text{m}$ vicinity) region. The simulated near-field intensities for all three orientations of the dipole over the glass and PC interface with and without AuNPs and AuNUs are presented in [Supplement 1](#) information ([Supplement 1](#) Figures S2–S4), and only a few representative examples are presented here. The steering far-field pattern is observed in the case of TE polarized scenario as seen in Figs. 3(a)–3(c). Further, steering and directional (highly angular) far-field patterns were observed for x -oriented (Figs. 3(d)–3(f)) and z -oriented (Figs. 3(g)–3(i)) dipoles, respectively. More importantly, the steering far-field pattern observed in the case of y and x -oriented dipoles presented quenching effects with the use of AuNPs (red curves in Fig. 3) and dequenching effects with AuNUs (yellow curves in Fig. 3), as evident from the near-field emission shown in Figs. 3(c) and 3(f). The z -oriented dipole yielded highly directional emission output with no significant quenching effects for AuNPs which is understandable due to the high efficiency coupling of dipoles oriented perpendicular to the surface of the metal. The simulated scattering cross sections of AuNU (blue curve) and AuNP (blue dashed curve) are presented in Figure S5. Notably, near 580 nm (wavelength corresponding to the emitter), the scattering cross section of AuNU is approximately one order of magnitude higher than that of AuNP. In the field of conventional metal-enhanced fluorescence (MEF) and the recently introduced plasmon-controlled fluorescence (PCF) by Lakowicz et al., two strategies are well-established for

achieving strong fluorescence enhancement of proximal fluorophores: (1) increasing the size of plasmonic nanoparticles and (2) introducing structural anisotropy. Both approaches lead to a substantial increase in the scattering component of the total extinction, thereby amplifying radiative decay rates and enhancing near-field effects [4,42,65,66]. In our simulations, we observed a similar trend where an order-of-magnitude increase in scattering for AuNU compared to AuNP was observed indicating significantly stronger near-field interactions. This enhancement is expected to boost not only MEF but also other surface-sensitive spectroscopies such as SERS and SEIRA. These simulation results provided a clear rationale for the experimental design and optimization described in the subsequent sections. By and large it is worth noting that the radiating dipoles induced a strong surface-localized field that can potentially propagate into the substrate of the PC into the far-field as steering emission, in line with our recent reports [3,67–69].

3. Results and discussion

The conceptual schematic of the quenching and dequenching effects of AuNPs and AuNUs is shown in Figs. 4(a) and 4(b) and the experimental photonic crystal-coupled emission (PCCE) results are presented in Fig. 4(c). Figure 4(d) presents four comparative fluorescence spectra that highlight the role of the PC and nanoparticle topology in modulating RhB emission. The PCCE–Blank spectrum represents RhB on the PC without NPs and establishes the background fluorescence arising solely from the PC–RhB structure. The PCCE–AuNPs spectrum shows reduced emission intensity due to non-radiative energy transfer pathways introduced by spherical AuNPs. In contrast, the PCCE–AuNUs spectrum exhibits enhanced fluorescence, attributed to the intensified local electromagnetic fields generated by the nanourchin morphology. The Free-space (FS) trace corresponds to RhB on a glass substrate and serves as an off-resonance control. Together, these spectra clarify that the observed enhancement originates from hybrid photonic–plasmonic coupling rather than intrinsic fluorescence variations of the dye or substrate. While the blank PC substrates presented ~24-fold fluorescence enhancement on account of the steering fluorescence output (detailed in our earlier works) [3], the use of AuNPs quenched the fluorescence output to ~9-fold. Such quenching effects arise on account of the direct electron transfer from the excited state of the radiating dipole to the plasmonic NP surface (due to the dielectric loss of metal) [59,70] resulting in non-radiative decay channels, based on which numerous turn-OFF - turn-ON based biosensing frameworks have been developed [16,26]. However, although an experimental effect termed ‘quenching’ has been studied for decades and rationalized as Förster resonance energy transfer (FRET) or nanomaterial surface energy transfer (NSET), and inner filter effect based on specifics of the system, only recently efforts have been focussed towards generating substrates that are quench-free [71,72]. Although fabricating an insulating decoupler coating over the plasmonic NPs can provide dequenching effects, it only overcomes the surface-induced quenching leaving the electromagnetic (radiation) driven quenching effects still unaddressed. In the past decade, the scanning tunnelling microscope (STM) induced luminescence (STML) experiments [73] and tip-enhanced photoluminescence (TEPL) [52] measurements demonstrated promising results with sub-nanometre resolution in single-molecule sensing. With these studies as primary motivation, here we attempted to use a cost-effective experimental setup (devoid of objectives and optical prisms) and use effective microscopic and mesoscopic engineering strategies using plasmonic AuNUs as model systems. While the plasmonic AuNPs yielded quenched ~9-fold fluorescence signal, the AuNUs presented dequenched ~140-fold fluorescence signal, with the enhancement and spectral intensity shown in Figs. 4(c) and 4(d) respectively. Incorporation of proximal AuNU resulted in fluorophores being dequenched (demonstrating enhanced fluorescence compared to the quenched state observed in AuNP).

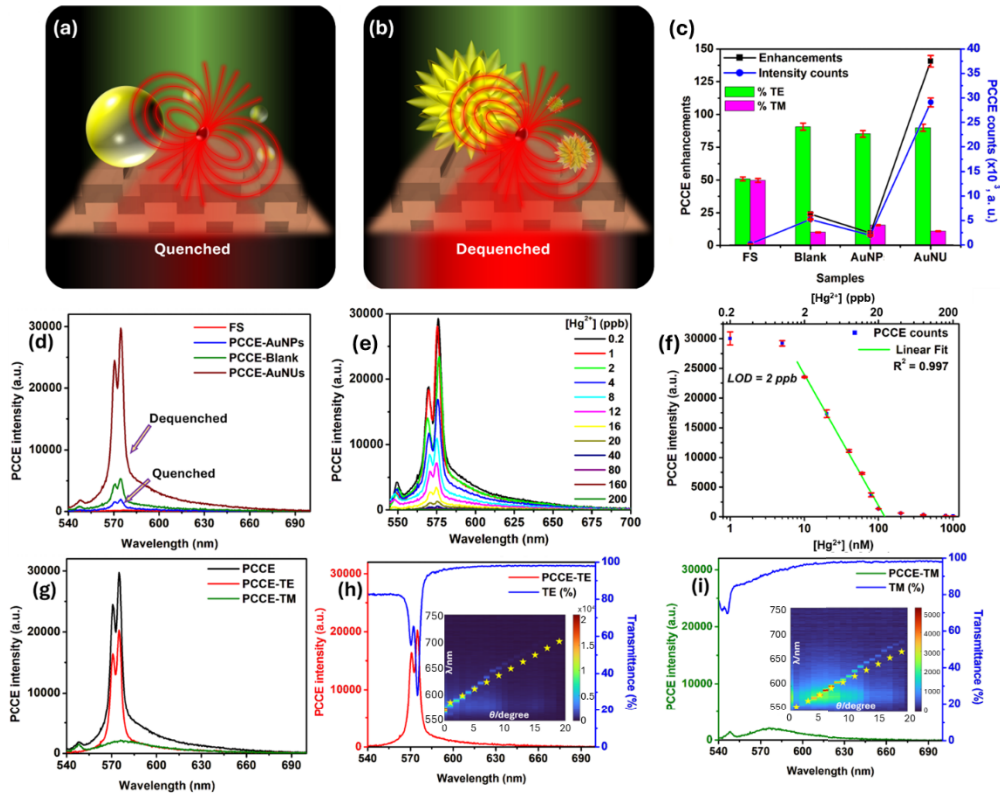


Fig. 4. Experimental realization of suppressed quenching and 2 ppb Hg^{2+} ion detection. Conceptual schematic of the coupling of radiating dipole with the (a) AuNPs and (b) AuNUs. (c) PCCE enhancements obtained experimentally for free space (FS), bank PC, PC with AuNPs and PC with AuNUs. (d) PCCE spectra with different combination, AuNPs-glass and PC; AuNUs-glass and PC. (e) PCCE, TM, TE out-coupled emission for AuNUs. (f) dispersion diagram overlap of the shaded experimental fluorescence with the dotted simulated data. The total emission power radiated by interfacing the AuNUs over the PC is shown as inset. Overlap of the experimentally obtained transmittance data with the experimentally obtained fluorescence spectra for (g) unpolarized output, (h) TE output, (i) TM output.

Using the plasmonic AuNUs – PC hybrid interface, a demonstration under controlled conditions was explored based on the interaction between rhodamine B and Hg^{2+} ions [74–76]. The sensing protocol was adopted from a recent report where a mixture of Hg^{2+} ions and potassium iodide in water yielded tetraiodomercurate which quenches the fluorescence of the rhodamine B [75]. Figure 4(e) presents the reduction in the fluorescence intensity observed with increasing concentration of the Hg^{2+} ions, the fluorescent counts given in Fig. 4(f) for concentration represented in molarity as well as in units of parts-per-billion (ppb). To establish a clear quantitative correlation, the normalized fluorescence intensity (I/I_0) was plotted against Hg^{2+} concentration. A linear relationship is observed for concentrations from 2 to 20 ppb, with a correlation coefficient of $R^2 = 0.997$, enabling accurate determination of Hg^{2+} levels. At lower concentrations (0.2–1 ppb), minimal changes in intensity were observed due to the sensitivity limits of the assay. This quantitative description confirms that the observed quenching is directly proportional to Hg^{2+} concentration and establishes the sensor’s linear dynamic range and limit of detection. While a low concentration of Hg^{2+} ions (0.2 and 1 ppb) did not yield a measurable change in the fluorescence intensity, higher concentrations (2 ppb to 20 ppb, with $R^2 = 0.997$)

showed significant reduction in the fluorescence signal thereby enabling a high linear range of sensing. While numerous methodologies have been employed for sensitive detection of Hg^{2+} ions, the 2 ppb limit of detection achieved in this report using the integrated hotspots from plasmonic AuNUs and all-dielectric PCs, shows sensor performance that is close to the reference concentration for drinking water (i.e., 2 ppb, as per EPA) and is lower than the permissible level recommended by WHO guideline (i.e., 6 ppb) [77]. While earlier studies have demonstrated the selectivity of the Rhodamine B- Hg^{2+} sensing approach against common interfering ions such as Mg^{2+} , Ca^{2+} , Na^+ , and K^+ , the current work focuses on demonstrating the fluorescence enhancement capability of AuNUs and its proof-of-principle performance in Hg^{2+} detection. Extensive ongoing studies in our laboratory are exploring sensor performance in real water samples and biological environments, including recovery analysis and selectivity across a wider range of potentially interfering species. These results will be included in future application-oriented work.

Different polarizers were used to understand the out-coupled fluorescence characteristics with associated experimental fluorescence spectral plots presented in Figs. 4(g)–4(i). The experimental fluorescence spectra for TE and TM present an excellent overlap with the experimental transmittance data collected at zero degrees. The experimental fluorescence collected at different angles (shaded region) were overlapped with the simulated reflectance values (stars) in the dispersion diagram presented as insets in Figs. 4h and 4i corresponding to TE and TM polarizations. Very interesting inferences may be drawn by carefully observing the experimental fluorescence (shaded region) and the far-field radiation pattern observed in the simulations (Figs. 3(b) and 3(c)) for different orientations of the dipole. From the simulations we noted that for the y -oriented dipole (contributing to the TE) the emission is predominantly directed towards the PC side as steering emission, and this is in excellent corroboration with the experimentally observed fluorescence output with the maximum fluorescence output seen as steering emission (here we refer to a zero-degree emission straight into the detector as steering emission) [3]. While this is straightforward in the case of TE-coupled emission, the insights that can be drawn for TM-coupled emission presents a reasonable deviation from the expectations. The x and z -oriented dipole together contribute to the TM-polarized out-coupled emission. From Figs. 3(e) and 3(f) we note that for the x -oriented dipole the emission shows a steering far-field pattern, the z -oriented dipole presents a highly angular (~ 45 degree) far-field emission. With this as simulation understanding, close observation of Fig. 4(i) (inset) shows an angular emission (~ 10 degrees) in accordance with the simulated data. The deviation in the angularity from ~ 45 degrees (in simulations) to ~ 10 degrees (in experiments) is attributed the ensemble averaging effect observed in experimental samples for TM polarization because of the x - and z - oriented dipoles render output in steering and directional patterns.

4. Outlook and conclusion

Further, it is informative to comment on the possible effects that support high fluorescence enhancement, simply by considering the path of the photons from laser to the detector. The steps may be summarized as follows: (i) the laser excites the dye molecules and the LSPR of the AuNUs simultaneously triggering the dye molecules to emit photons and the LSPR to generate intense field confinement, (ii) the AuNU-dye system is essentially a “plasmophore”, a system with plasmonic NPs in proximal distance from fluorophores [4,11,25,41]. Such systems present interesting effects from the perspective of theory of induced-plasmon effect of metal-enhanced fluorescence (MEF) [42]. On one hand the local field enhancement supported by the LSPR of AuNUs enhances the excitation intensity of proximal radiating dipoles. This is a well-known effect where the LSPR of plasmonic systems make provisions for enhancement factors of orders of magnitude (~ 5 -fold) that directly enhances the electronic transition probabilities (excitation) of proximal radiating dipoles, thereby enhancing the fluorescence in spite of surface-induced

quenching effects [16,21]. (iii) On the other hand, notably, the emitted photons from the radiating dipoles induces ultra-strong surface charge densities (plasmons) especially at the nano-protrusions in AuNUs, presenting newer radiative decay channels [78]. Such a hybrid system obeys the radiating plasmon model where the plasmonic NP and the radiating dipole emit as a ‘single hybrid entity’ rather than two separate entities, on account of the mutual excitation and enhancement effects. (iv) On account of the sharp protrusions of the AuNUs, the lightning rod effect assists in coupling of vertically and horizontally oriented radiating dipoles [52,73]. Moreover, the AuNU tip-core plasmon coupling augments the effective dipole moment of the tip plasmons, while the core of the AuNU serves as an antenna, enhancing the excitation cross sections and the electric field intensity [34]. Hence, the TE and TM polarized emission are enhanced from the plasmophore emission in the near-field (validated in Fig. 3). (v) Further the photons from plasmophore emission couples with the GMR of the underlying PC in accordance with the radiating GMR model carrying the spectral features of fluorophore and polarization selectivity of PC substrate. In our hybrid AuNU–photonic crystal system, TE- and TM-selective outcoupling enables fluorescence emission to be selectively directed through well-defined optical modes rather than isotropically radiating into free space (as observed for instance in the case of glass substrates). This property can be exploited to (i) improve signal-to-noise ratio by selectively collecting only the polarization channel associated with PC resonant enhancement, thereby suppressing background fluorescence/noise and scattering; (ii) enable multiplexed detection, where different fluorophores or targets can be engineered to couple to distinct polarized modes, allowing simultaneous discrimination of multiple analytes on a single substrate; (iii) simplify optical instrumentation for spectroscopy and microscopy (back focal plane imaging) by using polarization filtering in place of bulky wavelength- or angle-selective optics, improving suitability for compact PoC/PoU devices. Additionally, polarization-selective emission enables fundamental studies of anisotropic and polarization-sensitive materials, such as 2D materials, transition metal dichalcogenides, and other metamaterial-inspired systems, where polarization-linked optical transitions or direction-dependent dipole orientations can be probed with higher fidelity. Such capability offers a platform to correlate emission polarization with intrinsic material symmetry, excitonic coupling, or plasmonic–photonic hybridization mechanisms. As the emission travels only via the allowed modes of the PC (as in in dispersion diagrams), the collection efficiency is augmented as compared to the free space emission.

In summary, this work presents a simple route to overcome the quenching effects observed in AuNPs without incorporating an insulating layer into the synthesis of the nanoparticles. While the GMR of the PC is engineered to match the emission maximum of the radiating dipoles, the sharp protrusions in the AuNUs support coupling to differently oriented dipoles, thereby enhancing the TM and TE coupled emission. It is worth mentioning that this is the first report presenting a comprehensive analysis of radiating dipoles oriented in all three dimensions over the PC interface to draw conclusive remarks on the radiating GMR model. This synergistic effect of suppressed quenching by plasmonic AuNUs and high collection efficiency by the all-dielectric PC substrate presents unique quench-free interface, highly reliable for development of chem-biosensing technologies. While this study demonstrates the fluorescence enhancement and quenching suppression capabilities of AuNUs coupled with photonic crystals, further validation in complex matrices, including real water and biological samples, is currently underway to support future development of point-of-use and point-of-care sensing applications.

Funding. National Institutes of Health (R01AI159454, R01AI139401, R01CA227699, R01EB029805, U01AA029348); National Science Foundation (RAPID 20-27778, CBET 19-00277, CBET 22-32681).

Acknowledgement. Characterization was carried out in part in the Materials Research Laboratory Central Research Facilities, University of Illinois. S.B. acknowledges support from the Carl R. Woese Institute for Genomic Biology. J.T. was supported by the National Science Foundation Graduate Research Fellowship Program and the University of Illinois Distinguished Fellowship.

Disclosures. The authors have no conflict to disclose.

Data Availability. The data that support the findings of this study are available from the corresponding author upon reasonable request.

Supplemental document. See [Supplement 1](#) for supporting content.

References

1. *Principles of Fluorescence Spectroscopy* (Springer US, 2006).
2. C. H. Woo, S. Jang, G. Shin, *et al.*, “Sensitive fluorescence detection of SARS-CoV-2 RNA in clinical samples via one-pot isothermal ligation and transcription,” *Nat. Biomed. Eng.* **4**(12), 1168–1179 (2020).
3. S. Bhaskar, W. Liu, J. Tibbs, *et al.*, “Photonic crystal-coupled enhanced steering emission: A prism-free, objective-free, and metal-free loss-less approach for biosensing,” *Appl. Phys. Lett.* **124**(16), 161102 (2024).
4. J. R. Lakowicz, K. Ray, M. Chowdhury, *et al.*, “Plasmon-controlled fluorescence: a new paradigm in fluorescence spectroscopy,” *Analyst* **133**(10), 1308–1346 (2008).
5. N. Ganesh, W. Zhang, P. C. Mathias, *et al.*, “Enhanced fluorescence emission from quantum dots on a photonic crystal surface,” *Nat. Nanotechnol.* **2**(8), 515–520 (2007).
6. D. Thacharakkal, S. Bhaskar, T. Sharma, *et al.*, “Plasmonic synergism in tailored metal–carbon interfaces for real-time single molecular level sniffing of PFOS and PFOA,” *Chem. Eng. J.* **480**, 148166 (2023).
7. N. Jiang, X. Zhuo, and J. Wang, “Active Plasmonics: Principles, Structures, and Applications,” *Chem. Rev.* **118**(6), 3054–3099 (2018).
8. S. A. Maier, *Plasmonics: Fundamentals and Applications* (Springer US, 2007).
9. S. Bhaskar, A. K. Singh, P. Das, *et al.*, “Superior Resonant Nanocavities Engineering on the Photonic Crystal-Coupled Emission Platform for the Detection of Femtomolar Iodide and Zeptomolar Cortisol,” *ACS Appl. Mater. Interfaces* **12**(30), 34323–34336 (2020).
10. A. Pokhriyal, M. Lu, C. S. Huang, *et al.*, “Multicolor fluorescence enhancement from a photonics crystal surface,” *Appl. Phys. Lett.* **97**(12), 121108 (2010).
11. P. Barya, Y. Xiong, S. Shepherd, *et al.*, “Photonic-Plasmonic Coupling Enhanced Fluorescence Enabling Digital-Resolution Ultrasensitive Protein Detection,” *Small* **19**(44), 2207239 (2023).
12. P. C. Mathias, N. Ganesh, W. Zhang, *et al.*, “Graded wavelength one-dimensional photonic crystal reveals spectral characteristics of enhanced fluorescence,” *J. Appl. Phys.* **103**(9), 094320 (2008).
13. G. G. See, M. S. Naughton, L. Xu, *et al.*, “Enhanced emission of quantum dots embedded within the high-index dielectric regions of photonic crystal slabs,” *Appl. Phys. Lett.* **108**(17), 171108 (2016).
14. L. K. Acosta, C. S. Law, A. Santos, *et al.*, “Tuning intrinsic photoluminescence from light-emitting multispectral nanoporous anodic alumina photonic crystals,” *APL Photonics* **7**(2), 026108 (2022).
15. Y. Xiong, S. Shepherd, J. Tibbs, *et al.*, “Photonic Crystal Enhanced Fluorescence: A Review on Design Strategies and Applications,” *Micromachines* **14**(3), 668 (2023).
16. S. Bhaskar, N. C. S. S. Kowshik, S. P. Chandran, *et al.*, “Femtomolar Detection of Spermidine Using Au Decorated SiO₂ Nanohybrid on Plasmon-Coupled Extended Cavity Nanointerface: A Smartphone-Based Fluorescence Dequenching Approach,” *Langmuir* **36**(11), 2865–2876 (2020).
17. G. Damiano, B. Sara, J. Riccardo, *et al.*, “Prevention of Self-Quenching in Fluorescent Silica Nanoparticles by Efficient Energy Transfer,” *Angew. Chem.* **52**(23), 5965–5968 (2013).
18. N. Kongsuwan, A. Demetriadou, R. Chikkaraddy, *et al.*, “Suppressed Quenching and Strong-Coupling of Purcell-Enhanced Single-Molecule Emission in Plasmonic Nanocavities,” *ACS Photonics* **5**(1), 186–191 (2018).
19. K. A. Kang, J. Wang, J. B. Jasinski, *et al.*, “Fluorescence Manipulation by Gold Nanoparticles: From Complete Quenching to Extensive Enhancement,” *J. Nanobiotechnol.* **9**(1), 16 (2011).
20. J. Yang, R. Faggiani, and P. Lalanne, “Light emission in nanogaps: overcoming quenching,” *Nanoscale Horiz.* **1**(1), 11–13 (2016).
21. S. Bhaskar, P. Das, M. Moronshing, *et al.*, “Photoplasmonic assembly of dielectric-metal, Nd₂O₃-Gold core nanointerfaces for dequenching the luminophore emission,” *Nanophotonics* **10**(13), 3417–3431 (2021).
22. K. Saha, S. S. Agasti, C. Kim, *et al.*, “Gold Nanoparticles in Chemical and Biological Sensing,” *Chem. Rev.* **112**(5), 2739–2779 (2012).
23. M.-C. Daniel and D. Astruc, “Gold Nanoparticles: Assembly, Supramolecular Chemistry, Quantum-Size-Related Properties, and Applications toward Biology, Catalysis, and Nanotechnology,” *Chem. Rev.* **104**(1), 293–346 (2004).
24. K. M. Ganesh, S. Bhaskar, V. S. K. Cheerla, *et al.*, “Review of Gold Nanoparticles in Surface Plasmon-Coupled Emission Technology: Effect of Shape, Hollow Nanostructures, Nano-Assembly, Metal–Dielectric and Heterometallic Nanohybrids,” *Nanomaterials* **14**(1), 111 (2024).
25. K.-X. Xie, Q. Liu, X.-L. Song, *et al.*, “Amplified Fluorescence by Hollow-Porous Plasmonic Assembly: A New Observation and Its Application in Multiwavelength Simultaneous Detection,” *Anal. Chem.* **93**(8), 3671–3676 (2021).
26. V. S. K. Cheerla, K. M. Ganesh, S. Bhaskar, *et al.*, “Smartphone-Based Attomolar Cyanide Ion Sensing Using Au-Graphene Oxide Core Nanoassembly and Benzoxazolium-Based Fluorophore in a Surface Plasmon-Coupled Enhanced Fluorescence Interface,” *Langmuir* **39**(22), 7939–7957 (2023).
27. A. Rai, S. Bhaskar, K. M. Ganesh, *et al.*, “Gelucire®-mediated heterometallic AgAu nanohybrid engineering for femtomolar cysteine detection using smartphone-based plasmonics technology,” *Mater. Chem. Phys.* **279**, 125747 (2022).

28. C. Chen, L. Zhang, M. Yang, *et al.*, “Size and distance dependent fluorescence enhancement of nanoporous gold d,” *Opt. Express* **25**(9), 9901 (2017).
29. H. Yu, Y. Peng, Y. Yang, *et al.*, “Plasmon-enhanced light–matter interactions and applications,” *npj Comput. Mater.* **5**(1), 45 (2019).
30. J. B. Khurgin, “How to deal with the loss in plasmonics and metamaterials,” *Nat. Nanotechnol.* **10**(1), 2–6 (2015).
31. S. Jahani and Z. Jacob, “All-dielectric metamaterials,” *Nat. Nanotechnol.* **11**(1), 23–36 (2016).
32. C. Hrelescu, T. K. Sau, A. L. Rogach, *et al.*, “Single gold nanostars enhance Raman scattering,” *Appl. Phys. Lett.* **94**(15), 153113 (2009).
33. S. K. Dondapati, T. K. Sau, C. Hrelescu, *et al.*, “Label-free Biosensing Based on Single Gold Nanostars as Plasmonic Transducers,” *ACS Nano* **4**(11), 6318–6322 (2010).
34. F. Hao, C. L. Nehl, J. H. Hafner, *et al.*, “Plasmon Resonances of a Gold Nanostar,” *Nano Lett.* **7**(3), 729–732 (2007).
35. E. Prodan, C. Radloff, N. J. Halas, *et al.*, “A Hybridization Model for the Plasmon Response of Complex Nanostructures,” *Science* **302**(5644), 419–422 (2003).
36. H. Wang, D. W. Brandl, P. Nordlander, *et al.*, “Plasmonic Nanostructures: Artificial Molecules,” *Acc. Chem. Res.* **40**(1), 53–62 (2007).
37. Y. Gao, J. Wang, W. Wang, *et al.*, “More Symmetrical ‘Hot Spots’ Ensure Stronger Plasmon-Enhanced Fluorescence: From Au Nanorods to Nanostars,” *Anal. Chem.* **93**(4), 2480–2489 (2021).
38. Y. H. Su, W. H. Lai, W.-Y. Chen, *et al.*, “Surface plasmon resonance of gold nano-sea-urchin,” *Appl. Phys. Lett.* **90**(18), 181905 (2007).
39. S. A. Maier, M. L. Brongersma, P. G. Kik, *et al.*, “Plasmonics—A Route to Nanoscale Optical Devices,” *Adv. Mater.* **13**(19), 1501–1505 (2001).
40. M. Nyman, A. Shevchenko, I. Shavrin, *et al.*, “Large-area enhancement of far-field fluorescence intensity using planar nanostructures,” *APL Photonics* **4**(7), 076101 (2019).
41. M. Gharib, A. J. Yates, S. Sanders, *et al.*, “Golden Plasmonophores with Tunable Photoluminescence and Outstanding Thermal and Photothermal Stability,” *Adv. Opt. Mater.* **12**(14), 2302833 (2024).
42. J. R. Lakowicz, “Radiative decay engineering 5: metal-enhanced fluorescence and plasmon emission,” *Anal. Biochem.* **337**(2), 171–194 (2005).
43. M. H. Chowdhury, K. Ray, C. D. Geddes, *et al.*, “Use of silver nanoparticles to enhance surface plasmon-coupled emission (SPCE),” *Chem. Phys. Lett.* **452**(1-3), 162–167 (2008).
44. C. D. Geddes, *Surface Plasmon Enhanced, Coupled and Controlled Fluorescence* (John Wiley & Sons, 2017).
45. S. Bhaskar, P. Das, V. Srinivasan, *et al.*, “Plasmonic-Silver Soret and Dielectric-Nd₂O₃ nanorods for Ultrasensitive Photonic Crystal-Coupled Emission,” *Mater. Res. Bull.* **145**, 111558 (2022).
46. S. A. Maier and H. A. Atwater, “Plasmonics: Localization and guiding of electromagnetic energy in metal/dielectric structures,” *J. Appl. Phys.* **98**(1), 011101 (2005).
47. S. Grandi, M. P. Nielsen, J. Cambiasso, *et al.*, “Hybrid plasmonic waveguide coupling of photons from a single molecule,” *APL Photonics* **4**(8), 086101 (2019).
48. C. Chen, Y. Chen, Z. Fang, *et al.*, “Hybrid material integration for active photonic applications,” *APL Photonics* **9**(3), 030903 (2024).
49. A. Rai, S. Bhaskar, K. M. Ganesh, *et al.*, “Hottest Hotspots from the Coldest Cold: Welcome to Nano 4.0,” *ACS Appl. Nano Mater.* **5**(9), 12245–12264 (2022).
50. S. Bhaskar, S. M. Lis S, S. Kanvah, *et al.*, “Single-Molecule Cholesterol Sensing by Integrating Silver Nanowire Propagating Plasmons and Graphene Oxide π -Plasmons on a Photonic Crystal-Coupled Emission Platform,” *ACS Appl. Opt. Mater.* **1**(1), 159–172 (2023).
51. . “Comsol Multiphysics®,” (COMSOL AB, 2024).
52. B. Yang, G. Chen, A. Ghafoor, *et al.*, “Sub-nanometre resolution in single-molecule photoluminescence imaging,” *Nat. Photonics* **14**(11), 693–699 (2020).
53. M. Seo and J. W. Ha, “Effective surface-enhanced Raman scattering of randomly branched gold nano-urchins with Rhodamine 6G as Raman reporters,” *Microchem. J.* **140**, 47–51 (2018).
54. B. Ren, G. Picardi, and B. Pettinger, “Preparation of gold tips suitable for tip-enhanced Raman spectroscopy and light emission by electrochemical etching,” *Rev. Sci. Instrum.* **75**(4), 837–841 (2004).
55. L. Liu, S. Bhaskar, and B. T. Cunningham, “Hybrid interfacial cryosoret nano-engineering in photonic resonator in terferometric scattering microscopy: Insights from nanoparticles and nano-assemblies,” *Appl. Phys. Lett.* **124**(23), 234101 (2024).
56. Z. Y. Li, “Mesoscopic and Microscopic Strategies for Engineering Plasmon-Enhanced Raman Scattering,” *Adv. Opt. Mater.* **6**(16), 1701097 (2018).
57. W. Ahmed, İM Öztürk, R. M. F. Iftikhar, *et al.*, “Seedless, size and shape controlled synthesis of gold mesoscopic particles and their excellent SERS applications,” *Mater. Chem. Phys.* **278**, 125589 (2022).
58. S. Kim, S. Yoo, D. H. Nam, *et al.*, “Monodispersed mesoscopic star-shaped gold particles via silver-ion-assisted multi-directional growth for highly sensitive SERS-active substrates,” *Nano Convergence* **11**(1), 26 (2024).
59. J.-Z. Zhu, G. Chen, T. Ijaz, *et al.*, “Influence of an atomistic protrusion at the tip apex on enhancing molecular emission in tunnel junctions: A theoretical study,” *The Journal of Chemical Physics* **154**(21), 214706 (2021).
60. S. A. Schulz, R. F. Oulton, M. Kenney, *et al.*, “Roadmap on photonic metasurfaces,” *Appl. Phys. Lett.* **124**(26), 260701 (2024).

61. R. Badugu, S. Blair, E. Descrovi, *et al.*, "Fluorophore interactions with the surface modes and internal modes of a photonic crystal," *Opt. Mater.* **147**, 114718 (2024).
62. P. Gupta, "Controlling Level Splitting by Strong Coupling of Surface Plasmon Resonances with Rhodamine-6G on a Gold Grating," *Plasmonics* **13**(6), 2067–2077 (2018).
63. R. Badugu, J. Mao, S. Blair, *et al.*, "Bloch Surface Wave-Coupled Emission at Ultraviolet Wavelengths," *J. Phys. Chem. C* **120**(50), 28727–28734 (2016).
64. S. Bhaskar, V. Srinivasan, and S. S. Ramamurthy, "Nd₂O₃-Ag Nanostructures for Plasmonic Biosensing, Antimicrobial, and Anticancer Applications," *ACS Appl. Nano Mater.* **6**(2), 1129–1145 (2023).
65. J. R. Lakowicz, "Plasmonics in Biology and Plasmon-Controlled Fluorescence," *Plasmonics* **1**(1), 5–33 (2006).
66. J. R. Lakowicz and Y. Fu, "Modification of single molecule fluorescence near metallic nanostructures," *Laser Photonics Rev.* **3**(1-2), 221–232 (2009).
67. S. Bhaskar, L. Liu, W. Liu, *et al.*, "Photonic crystal band edge coupled enhanced fluorescence from magneto-plasmonic cryosoret nano-assemblies for ultra-sensitive detection," *APL Mater.* **13**(4), 041103 (2025).
68. S. Bhaskar, W. Wang, H. Lee, *et al.*, "Photonic Crystal Grating Resonance and Interfaces for Health Diagnostic Technologies," *Chem. Rev.* **125**(14), 6435–6540 (2025).
69. S. Bhaskar, L. Liu, W. Liu, *et al.*, "Photonic-crystal-enhanced fluorescence: Template-free gold cryosoret nanoassembly steering, dequenching, and augmenting the quenched emission from radiating dipoles," *MRS Bull.* **50**(5), 585–598 (2025).
70. R. R. Chance, A. Prock, and R. Silbey, "Molecular Fluorescence and Energy Transfer Near Interfaces," in *Advances in Chemical Physics* I. Prigogine and S. A. Rice, eds. (Wiley, 1978), pp. 1–65.
71. C. Chen and N. Hildebrandt, "Resonance energy transfer to gold nanoparticles: NSET defeats FRET," *TrAC Trends in Analytical Chemistry* **123**, 115748 (2020).
72. T. T. Trang, T. T. H. Pham, N. V. Dang, *et al.*, "Revealing the high efficiency of fluorescence quenching of rhodamine B by triangular silver nanodisks due to the inner filter effect mechanism," *RSC Adv.* **14**(14), 9538–9546 (2024).
73. L. Zhang, Y.-J. Yu, L.-G. Chen, *et al.*, "Electrically driven single-photon emission from an isolated single molecule," *Nat. Commun.* **8**(1), 580 (2017).
74. S. K. Gupta, K. Tapadia, and A. Sharma, "Selective Fluorometric Analysis of Hg(II) in Industrial Waste Water Samples," *J. Fluoresc.* **30**(6), 1375–1381 (2020).
75. S. M. Radiul and S. Hazarika, "A selective and sensitive mercury sensor for drinking water based on fluorescence quenching of pure rhodamine B," *Laser Phys.* **34**(8), 085602 (2024).
76. Z. Wang, M. Yang, C. Chen, *et al.*, "Selectable Ultrasensitive Detection of Hg²⁺ with Rhodamine 6G-Modified Nanoporous Gold Optical Sensor," *Sci. Rep.* **6**(1), 29611 (2016).
77. Q. Wei, R. Nagi, K. Sadeghi, *et al.*, "Detection and Spatial Mapping of Mercury Contamination in Water Samples Using a Smart-Phone," *ACS Nano* **8**(2), 1121–1129 (2014).
78. S. Bhaskar, R. Patra, N. C. S. S. Kowshik, *et al.*, "Nanostructure effect on quenching and dequenching of quantum emitters on surface plasmon-coupled interface: A comparative analysis using gold nanospheres and nanostars," *Physica E: Low-dimensional Systems and Nanostructures* **124**, 114276 (2020).